POLITECNICO
MILANO 1863

RE.PUBLIC@POLIMI
Research Publications at Politecnico di Milano

**Post-Print**

This is the accepted version of:

L. Pernigoni, A.M. Grande
*Development of a Supramolecular Polymer Based Self-Healing Multilayer System for Inflatable Structures*
Acta Astronautica, Vol. 177, 2020, p. 697-706
doi:10.1016/j.actaastro.2020.08.025

The final publication is available at https://doi.org/10.1016/j.actaastro.2020.08.025

Access to the published version may require subscription.

**When citing this work, cite the original published paper.**

© 2020. This manuscript version is made available under the CC-BY-NC-ND 4.0 license
http://creativecommons.org/licenses/by-nc-nd/4.0/

Permanent link to this version
http://hdl.handle.net/11311/1145732

Manuscript File Click here to view linked References

# Development of a supramolecular polymer based self-healing multilayer system for inflatable structures

Laura Pernigoni[a,*], Antonio M. Grande[a]

[a] *Department of Aerospace Science and Technology, Politecnico di Milano, via La Masa 34, Milano 20156, Italy*

[*] Corresponding author.
E-mail addresses: laura.pernigoni@polimi.it, antoniomattia.grande@polimi.it

**Abstract**

*Self-healing materials have become more and more interesting for the space industry, since they can lead to the creation of space systems and structures able to repair autonomously after accidental damages caused by collision with micrometeoroids and orbital debris during the entire operational life. The implementation of these novel materials results in higher protection and safety for astronauts, and longer missions in the perspective of lunar bases establishment and manned exploration of Mars.*

*The present study aims to experimentally and numerically characterize an intrinsic self-healing supramolecular polymer that is potentially applicable to space suits, habitats and inflatable structures in general. A dedicated test device has been developed to evaluate the sealing performance of the material through flow rate measurements after a puncture event. The experimental part is followed by the study of the material's constitutive relations including hyperelastic and viscoelastic responses. The related model parameters are computed and calibrated through optimization and data matching tools in order to simulate damage and healing events.*

*Results show that the selected supramolecular polymer possesses effective self-healing abilities also under pressurized conditions, demonstrating its applicability to the considered specific fields in the space sector. Furthermore, for what concerns the analyzed puncture experiments and field of solicitation, the developed model can follow the relaxation process related to the self-healing behavior, since it can predict whether the material is effectively able or not to flow and repair.*

*Keywords:* inflatable space structures; self-healing; supramolecular polymers; multilayer systems

**Nomenclature**

| | | | |
|---|---|---|---|
| DGEBA | Diglycidyl ether of bisphenol A | $r$ | Radius [mm] |
| EMU | Extravehicular Mobility Unit | $R_a$ | Gas constant of air [J/kg/K] |
| EVA | Extravehicular Activity | $r_f$ | Final hole radius [mm] |
| MMOD | Micrometeoroid and Orbital Debris | $r_p$ | Puncture probe radius [mm] |
| TRL | Technology Readiness Level | $t$ | Time [s] |
| $a$ | Initial hole radius [mm] | $T_0$ | Cylinder absolute internal temperature [K] |
| $A_h$ | Equivalent hole area [mm$^2$] | $T_i$ | Simulation steps periods (i=1,2,3) [s] |
| $C_d$ | Discharge coefficient [-] | $U$ | Strain energy per unit ref. volume [MPa] |
| $C_{i0}$ | Yeoh model parameter [MPa] | $u_r$ | Radial displacement [mm] |
| $D_i$ | Yeoh model parameter [MPa$^{-1}$] | $v_p$ | Puncture probe approximate speed [mm/s] |
| $g$ | Normalized modulus (Prony series) [-] | $v_r$ | Radial velocity [mm/s] |
| $g_i$ | Prony series normalized constants [-] | $\gamma$ | Air specific heat ratio [-] |
| $h_p$ | Puncheon's sharp edge height [mm] | $\Delta t_h$ | Time from null to max. puncture radius [s] |
| $\bar{I}_1$ | First deviatoric strain invariant [-] | $\varepsilon$ | Strain [-] |
| $J_{el}$ | Elastic volume ratio [-] | $\rho_a$ | Air density [kg/m$^3$] |
| $\dot{m}$ | Mass flow rate [kg/s] | $\sigma$ | Stress [MPa] |
| $p_0$ | Cylinder absolute internal pressure [MPa] | $\tau_i$ | Prony series characteristic times [s] |
| $p_a$ | Ambient pressure [MPa] | $\psi$ | Outflow function [-] |
| $Q$ | Volumetric flow rate [l/min] | | |

## 1. Introduction

Inflatable structures such as habitats, airlocks, space suits and ballutes will gain more importance in future space explorations [1,2]. Their advantages are related to a high packing efficiency, low mass and launch costs and reliable expandable volumes [3]. Nevertheless, while operating in space the integrity of these systems will be threatened by vacuum, absence of atmosphere, radiation, micrometeoroids and orbital debris (MMOD) and extreme thermal solicitations [4]. In particular, MMOD impacts and accidental contact with sharp objects can generate punctures and cuts and cause gas leakage and depressurization [5,6]. Since at present no space systems can autonomously repair, events of this type will have catastrophic effects.

In the space field damage tolerance design is extensively used in the development of advanced structures. However, in a number of situations including non-structural applications, presence of damage may remarkably impair the functionality or lifetime of the component. The development of new materials with improved strength and durability linked to new functionalities can answer to the request of safer, lighter and more reliable space structures [4,7].

Polymers ~~and elastomers~~ are widely employed in various space applications in structures, seals, damping elements, and joints. These systems are subjected to severe and complex load conditions as multi-axial loading, fatigue, impact, abrasion, and wear [1,4,8]. It is hence conceivable that damages occurring during their service life can potentially lead to catastrophic failure of the entire structure. These materials are employed in various critical applications such as space suits and space living habitats, liquid propellant containers, inflatable objects and also protective coatings, optical surfaces, conductive or resistive materials, where material continuity is a stringent requirement. When used in space applications, human intervention for the repair of the damaged components is dangerous, costly or even impossible [7].

In this view, the implementation of the self-healing principle to space systems would be beneficial to increase reliability and reduce maintenance costs. The self-healing concept is based on a damage management principle: once damage has occurred the material should be able to repair itself partially or totally with none or low external intervention, so that its main functionality is restored [9]. Although several chemical concepts have been used to develop self-healing polymers, no commercially available polymer ~~or elastomer~~ has been reported for space applications combining both high mechanical properties and a substantial healing efficiency. One of the reasons for such gap is the relatively low understanding of the healing phenomena and the lack of robust techniques capable of characterizing the true healing potential of self-healing polymers in space environment. New characterization approaches that give more relevant information about the healing mechanisms are required in order to make use of such new materials in the design of non-conventional space structures, such as inflatable ones. It becomes thus clear that the selection of a proper test and/or the combination of phenomenologically different tests is a necessary step for the development of new self-healing polymers with improved properties [8].

Being able to immediately seal ruptures would hence mean providing longer operational life, greater protection and increased safety for astronauts during human spaceflights. This could extend the duration of future missions [5], also in view of projects as manned exploration of Mars [10]. An example is given by the current Extravehicular Mobility Unit suits' emergency system, which has a limited autonomy of approximately 30 minutes. As a consequence, if damage from MMOD impact occurs during an Extravehicular Activity (EVA) the astronaut's life is seriously threatened by possible leakage and consequent suit's depressurization [5,11].

In this context, the integration of self-healing materials to space inflatable systems has become more and more appealing. Several passive self-healing mechanisms have been developed in the last years, but only few of them are currently being considered for space applications [8,12] (**Table 1**).

**Table 1:** Example of self-healing mechanisms considered for space applications.

| Mechanism | Category | References |
|---|---|---|
| Chemical reaction | Microspheres | [13–17] |
| | Filled hollow fibers | [14] |
| Environmental reaction | Material foams/gels in vacuum | [13] |
| | Microspheres | [13,14] |
| | Filled hollow fibers | [13] |
| | Protective films | [18,19] |
| Mechanical coverage | Closed cell foam | [20] |
| Flowing materials | Micro-vascular systems | [21] |
| | Viscoelastic gels | [22] |
| | Hydrogels | [23] |
| | Heat flow (EMAA) | [13] |
| | Supramolecular materials | [24] |
| Combined mechanisms | Environmental reaction + heat flow | [25] |
| | Hybrid microcapsule-microvascular systems | [26] |

In the chemical reaction mechanisms two materials are initially embedded inside thin flexible films. They are released and come into reciprocal contact after the creation of a damage, such as a puncture. The result is an exothermic reaction that allows healing of the generated void [27]. This concept may be potentially lightweight and thin, but it carries the risks of short shelf life and exothermal reaction severity.

The environmental reaction concept is very similar to the chemical one, but in this case a single reactant is encapsulated and activated by catalysts present in the environment (e.g.: oxygen, water) [25]. Another example is given by materials that foam under the action of vacuum. A positive aspect is given by their low density in relation to the repairable hole size, but this concept has a very low TRL, especially if compared to other mechanisms such as flowing or mechanical coverage materials. Other disadvantages are given by the unknown effects of by-products from outgassing, possible risks related to exothermal reactions and shelf life limitations [5].

The mechanical coverage idea relates on the presence of a material on the pressure side of the bladder or between the bladder and restraint of an inflatable system. The material flows or expands to fill the void that has been generated. An example is given by a compressed closed cell foam that expands after rupture while compressive loads are locally released. This simple mechanism relies on existing and sufficiently low-cost technology, it can be lightweight and resistant to folding and deployment [20]. Negative aspects are related to possible permanence of the seal and risk of compression set in the specific case of cell foams.

The present study focuses on passive intrinsic materials with viscoelastic properties, belonging to the flowing materials category (**Figure 1**). Together with reactive substances and foams, this is one of the most promising self-healing families.
A material flows into the hole created after rupture of a bladder layer and eventually seals it. This mechanism uses already existing and relatively affordable technologies that may be applied to a space suit's bladder. A further aid would be given by the pressure difference between the suit's internal part and the outer space, causing compression and transverse flow of the material. Nonetheless, possible disadvantages may be given by mass and reduced strength [5].

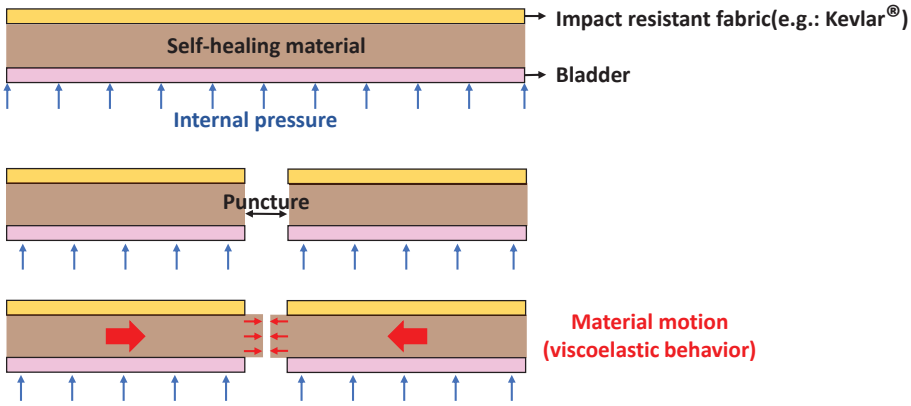

**Figure 1:** Self-healing viscoelastic material concept.

The paper describes the experimental and numerical characterization of a supramolecular intrinsic self-healing material applied to inflatable structures. The dedicated test apparatus has been adopted to evaluate the sealing performance of the material after a puncturing damage and flow rate measurement is selected as benchmark parameter. The testing apparatus is pressurized with continuous air supply to reproduce the inflatable system's internal conditions. Maximum and minimum flow rate, the time between them and the air volume lost in a reference time are used as performance indicators.
The developed testing procedure for the evaluation of the healing performances was applied to a commercially available self-healing supramolecular polymer (Reverlink® HR, Arkema). This polymer contains both strong irreversible covalent cross-links and weak reversible chemical bonds (hydrogen bonds) responsible for the self-healing functionality. Furthermore, its combined intrinsic and autonomic properties lead to a material which does not need neither a healing agent nor an external trigger to obtain the self-healing response [28].

The field of EMU space suits is used as a case study. Multilayer configurations are analyzed, combining the self-healing material with aramid fabrics and polyamide films.

## 2. Materials and methods

### *2.1. Materials*

The supramolecular polymer Reverlink® HR, containing epoxy-based networks, was provided by Arkema. The material possesses both chemical and supramolecular hydrogen-bonded crosslinks and is obtained from the DGEBA (di-glycidyl ether of bisphenol A prepolymer) [29, 30]. The specimens of the supramolecular material were prepared following the procedure recommended by the manufacturer. The provided pre-polymer was heated at around 80 °C and casted in a shaped PTFE mold. Subsequently the mold was heated in a standard oven at 120 °C for 24 hours in order to complete the curing of the polymer.

The tested multi-layered samples are composed by an aramid fabric (SAATI Style 101, areal weigh 460 g/m$^2$) and a polyamide film with thicknesses of 630 µm and 50 µm, respectively. These different layers were chosen to replicate the EMU configuration and to compare the related results with data and materials from the research on self-healing space suits carried out in a previous research [10]. As a matter of fact, the polyamide film reproduces the suit's bladder, while the aramid fabric represents the ripstop, impact-resistant part. The supramolecular polymer is embedded in between aramid fabric and polyamide film as self-healing layer.

### *2.2 Samples preparation*

Two multi-layer configurations were investigated. In the first one, the self-healing polymer prepared according to manufacture specification is initially shaped into a disk of 2.5 cm radius and kept between two

50 µm thick polyamide films (**Figure 2**). This multilayer configuration was adopted for the comparison between the simulated punctures and the experimental results.
In the second configuration, the aramid fabric substitutes the upper polyamide film (**Figure 3**). This fabric is introduced to study possible effects on healing performance due to the EMU outermost ripstop component [31].
In all cases, the material's disks thicknesses measure 1200±250 µm. All tests are performed by puncturing the central part to obtain their highest possible coherency and repeatability. Furthermore, to guarantee improved healing performances and complete water removal [28], the material is thermally treated at 50 °C for one week before being tested.

Dog-bone specimens of the self-healing polymer (ASTM 1708) were also prepared for tensile and relaxation tests used for the development of the material constitutive equation.

(a) (b)

**Figure 2:** Polyamide film lay-up schematization (a) and SH material between polyamide film layers (b).

(a) (b)

**Figure 3:** Polyamide film-aramid fabric lay-up schematization (a) and SH Material between polyamide and aramid fabric layers (b).

*2.3. Test fixture for healing performance evaluation*

The healing properties are experimentally determined with a dedicated test device (**Figure 4**)**.** Its main part is a pressure vessel consisting of a hollow cylinder with a bottom cap and a sealing ring on the top. The latter blocks the sample on the cylinder itself, allowing over pressurization of the internal cavity with respect to the external ambient. O-rings are used in cap and ring connections to avoid air leakage, and a puncture probe is used to keep a 2 mm diameter puncheon in place and pierce the sample during tests, creating an outward air flow from the generated hole. The probe is held by grips and set in motion by an MTS 858 Mini Bionix II® machine.
Two threaded holes are made on the cylindrical body as a connection with the instruments that measure flow rate and relative pressure. A pressure transducer is directly screwed to the cylindrical body and monitors the relative pressure inside the vessel, while a flow meter is set between the cylinder and the pneumatic supply line and connected to them through fittings and flexible tubes. It measures the air getting from the feed line to the cylinder and passing through its body. A precision pressure regulator and a finger valve are also present.

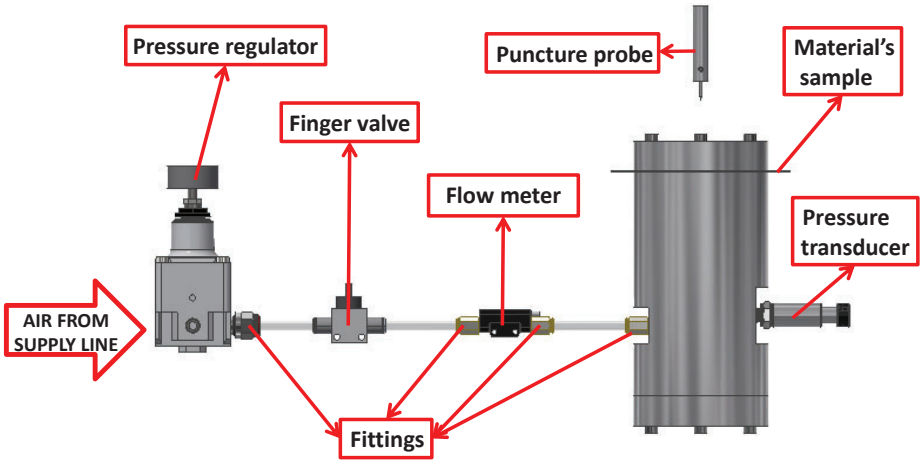


**Figure 4:** CAD representation of the testing system.

*2.4. Puncture tests*

For both sample types, three puncture test repetitions are carried out in a working environment at ambient conditions. The vessel is initially pressurized to 0.3 bar relative pressure to reproduce the space suit's conditions [32] and placed on the test machine support, above which the puncture probe is fixed. Air is continuously supplied from the feedline to the system and the puncheon is then set in motion, generating a hole in the studied sample. The volumetric flow rate through the sensor, which is approximately equal to the flow rate of air exiting from the orifice, is acquired during the test and processed with the LabVIEW® software. Null values of this quantity correspond to effective closure of the generated hole. Standard test ASTM F1342 is followed for the dimensions and velocity of the puncheon. All the tests were performed at room temperature.

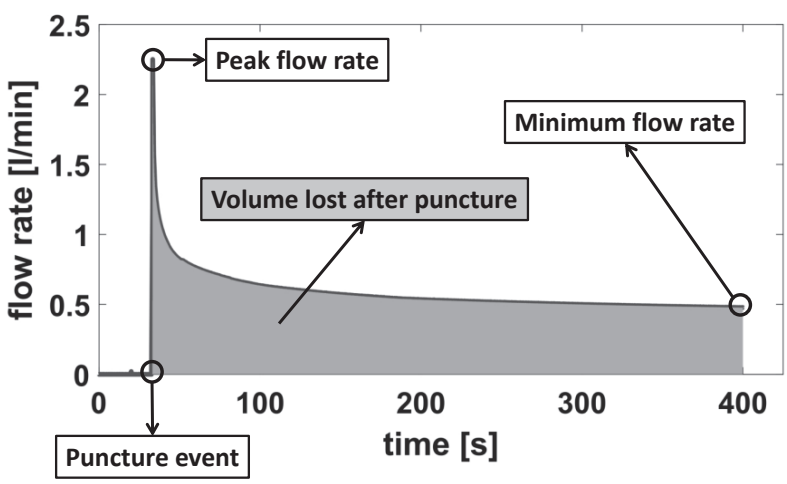


**Figure 5:** Example of flow rate curve and relative parameters for healing assessment.

The maximum and minimum flow rates and the volume lost in 180 s after puncture are evaluated to have an indication of the material's healing behavior (**Figure 5**), along with the time required to get from maximum to minimum flow rate. The trapezoidal rule is exploited for each curve to numerically integrate the flow rate over time and compute the volumes.

*2.5. Tensile and relaxation tests*

The mechanical and viscoelastic behavior of the self-healing material under small and large uniaxial deformations were studied experimentally for different loading conditions. To this aim, uniaxial tensile tests, as well as stress relaxation experiments were performed at different strain rates and maximal strain level on an Instron Model 3365 universal testing systems equipped with a 1 kN load cell. Tensile specimens were stretched at different constant crosshead speeds ranging from 0.1 mm/s to 1 mm/s. Relaxation tests were carried out in tensile mode by stretching the dog-bone samples at 1 mm/s up to 5%, 25% and 50% strain level and by following stress evolution in time for 3600 s. All tests were performed at room temperature.

*2.6. Numerical model*

A combined hyperelastic Yeoh-viscoelastic Prony series representation is used to model the material's behavior. Linear viscoelastic approximation is employed. After the evaluation of a suitable initial guess, the involved parameters are calibrated through fitting of tensile loading and relaxation curve. Tensile results are also used to obtain the starting hyperelastic parameters through the Abaqus® material evaluation tool. The stress relaxation tests at 5%, 25% and 50% strain are exploited to compute a preliminary estimation of the Prony terms. In particular, the 25% strain relaxation test curve is used for the determination of the $g_i$ and $\tau_i$ parameters. The Prony series expression is [33]:

$$g(t) = 1 - \sum_{i=1}^{5} g_i \cdot (1 - e^{-t/\tau_i}) \tag{1}$$

Concerning the hyperelastic contribution, Yeoh formulation is selected as a suitable representation [34]. The strain energy potential *U* is [33]:

$$U = C_{10} \cdot (\bar{I_1} - 3) + C_{20} \cdot (\bar{I_1} - 3)^2 + C_{30} \cdot (\bar{I_1} - 3)^3 + \frac{1}{D_1} \cdot (J_{el} - 1)^2 + \frac{1}{D_2} \cdot (J_{el} - 1)^4 + \frac{1}{D_3} \cdot (J_{el} - 1)^6 \tag{2}$$

A multiobjective optimization is run starting from the initial guess values and considering the experimental curves. For each of them an Abaqus® file containing a 3D model of the test specimen is created, run and inserted in Isight® along with the resulting output file, the optimization tool and the data matching feature. The 3D geometry used for the specimen follows the D1708 ASTM standard and exploits symmetry and simplifications to decrease the computational time. The grip sections are approximated as rigid bodies in the lower and upper surfaces, respectively (**Figure 6**).
Since the values of interest are the engineering stress and strain, reaction force and displacement are the optimization targets. Isight® iteratively runs the Abaqus® files and compares the simulation and the experimental results. The sums of the square differences, one for each deformation rate, are set as equally weighted objective functions and optimized with the Hooke-Jeeves technique [34]. This algorithm is a penalty pattern-search method which does not require the computation of gradients and works well when the initial feasible design is undetermined.
Calibration involves the $C_{i0}$ Yeoh constants and the $\tau_i, g_i$ Prony coefficients, for a total of 13 variables. Constraints are introduced to grant hyperelastic stability and respect the Prony series definition [33]:

- Yeoh model stability: $C_{i0} > 0$
- Prony constants: $0 < g_i < 1,\ \sum_{i=1}^{5} g_i \leq 1$
- Prony characteristic times: $\tau_i > 0\ s$

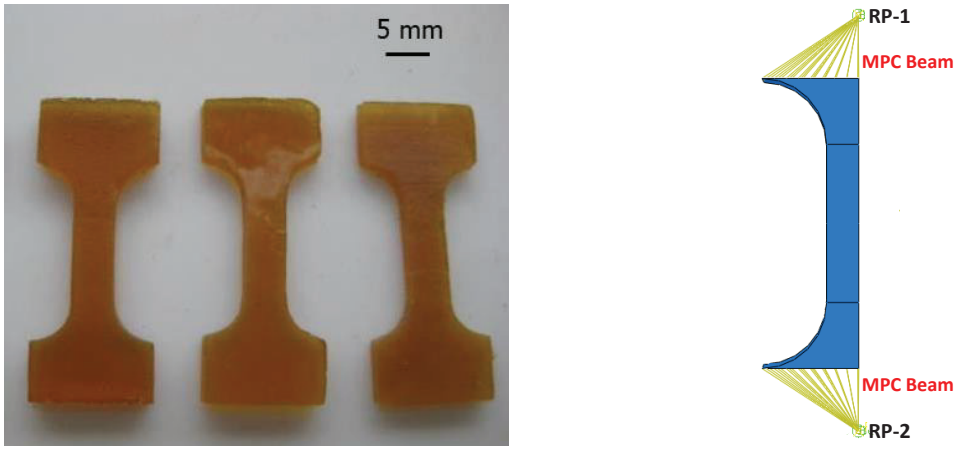


(a) (b)

**Figure 6:** Tested tensile and relaxation samples (a) and 3D specimen model (b).

*2.7. Puncture simulation*

The optimized material parameters are used to simulate response to puncture. For the sake of simplicity, the case without fabric is taken as reference configuration. A 2D geometrical model of the specimen is developed by exploiting symmetries, allowing to consider only one fourth of a disk with 50 mm diameter. Motion at its boundaries is set to zero to account for the sealing ring that keeps the specimen in place during the tests. The polyamide film layers are not inserted in the model, since they do not provide significant mechanical contribution to the material and can hence be neglected. Contact and rupture are not modeled either; on the other hand, a small hole with initial radius $a$ is inserted in the disk. A reasonable value to avoid excessive element distortion is $a$=0.2 mm.
The hole's maximum radial displacement $u_{r,max}(a)$ is imposed by the radius $r_p$ of the puncheon penetrating the sample:

$$u_{r,max}(a) = r_p - a \tag{3}$$

Analyzing the 2 mm puncture case with $a$ = 0.2 mm, it is found that $u_{r,max}(a) = 0.8$ mm.

Due to the 2D approximation, the dependence of the hole dimensions on the position along the specimen's thickness is lost. When considering a certain instant before complete penetration, in the real situation only some zones are punctured, depending on the position along the thickness. The radius is not constant along it, except for the time during which the probe's sharp edge has completed its downward motion through the whole specimen and has not started its upward motion yet. Another neglected aspect is the action on the specimen of pressure given by the 0.3 bar difference between the cylinder and the outer environment.

The simulation is divided into three steps representing the puncture test phases. In the first one the puncheon penetrates the material's sample, following the assumption that the hole's radial displacement linearly varies in time from $u_r(a, 0\ s)$=0 mm to $u_{r,max}(a)$=0.8 mm. The step period is related to $u_{r,max}(a)$. The vertical velocity imposed to the puncheon comes from standard indications [35]:

$$v_p = 50.8\frac{cm}{min} \cong 8.46\ mm/s \tag{4}$$

The hole gets to its maximum dimensions once the puncture probe's sharp end has completely penetrated the material. For this reason, the time from null to final radius is seen as the one required by the puncheon to travel a distance equal to the sharp edge's height $h_p = 3.53$ mm:

$$\Delta t_h = \frac{h_p}{v_p} \cong 0.42\ s \tag{5}$$

Radial velocity can be computed as:

$$v_r = \frac{r_{,max}}{\Delta t_h} \cong 2.40\ mm/s \tag{6}$$

Due to the non-null initial radius approximation, the first step period coincides with the time in which the radius itself gets from 0.2 mm to 1 mm:

$$T_1 = \frac{u_{r,max}}{v_r} \cong 0.33\ s \tag{7}$$

The second time step indicates the phase in which the puncheon has completely pierced the material and is still inside it. The hole is forced to remain to its $r = 1$ mm maximum dimension, and partial stress relaxation occurs. An acceptable estimate of the step is $T_2 \cong 0.45$ s.

In the last step the motion constraint on the hole is removed, causing it to gradually get back to its initial dimensions. The relaxation time is set equal to the interval between maximum flow rate and final acquisition in the tests: $T_3 = 380$ s.
Quad-dominated plane stress elements are considered for the meshing scheme (**Figure 7**), using the sweep technique to follow the circular shape of the specimen. Since the hole is subject to considerable deformation and has very small initial dimensions a finer meshing scheme is adopted in its proximity, in the attempt of avoiding excessive distortion.

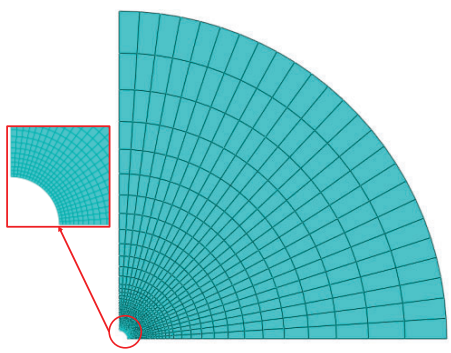

**Figure 7:** Mesh scheme for puncture simulation.

The radial displacement obtained from the simulation is then used to compute the air flow rate, as will be described in the results section.

## 3. Results

### *3.1. Puncture experiments*

The data from puncture tests are indicated in **Figure 8**. The configuration with the aramid fabric (b) shows significant improvements both in terms of peak flow rate and self-healing rate when compared to the case with polyamide films only (a). It is particularly evident that the addition of the ripstop layer leads to an important decrease of the healing time. As a matter of fact, this case shows a general excellent healing behavior, with complete hole closure in less than a minute in two cases out of three. In the best repetition complete hole closure is reached in approximately 52.3 s with a 46 $cm^3$ volume loss.

For what concerns the specimen with polyamide films, the sealing response is related to the saturation of the flowmeter to its maximum measurable flow rate of 3 l/min. Flow rate then stabilizes around 0.05 l/min in all the repetitions when approaching the end of the test.

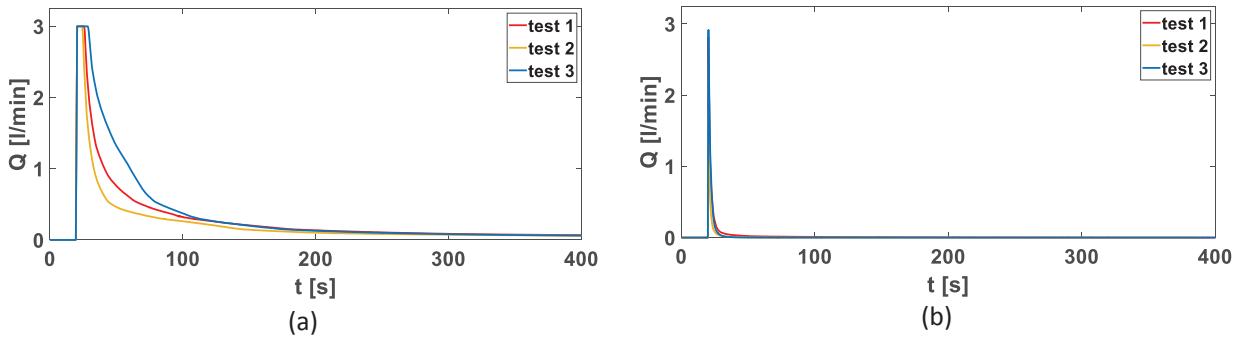


**Figure 8:** Volumetric flow rate from puncture tests, cases without aramid fabric (a) and with aramid fabric (b).

A leakage test is also performed two hours after puncture to verify ~~sealing~~ complete healing of the samples: the volumetric flow rate is acquired while a relative pressure variation from 0.3 to 0.8 bar is imposed (**Figure 9**). For every pressure step, after a jump due to the initial imbalance between the cylindrical vessel and the feed line, the flow rate quickly decreases and ultimately reaches values comparable to zero.

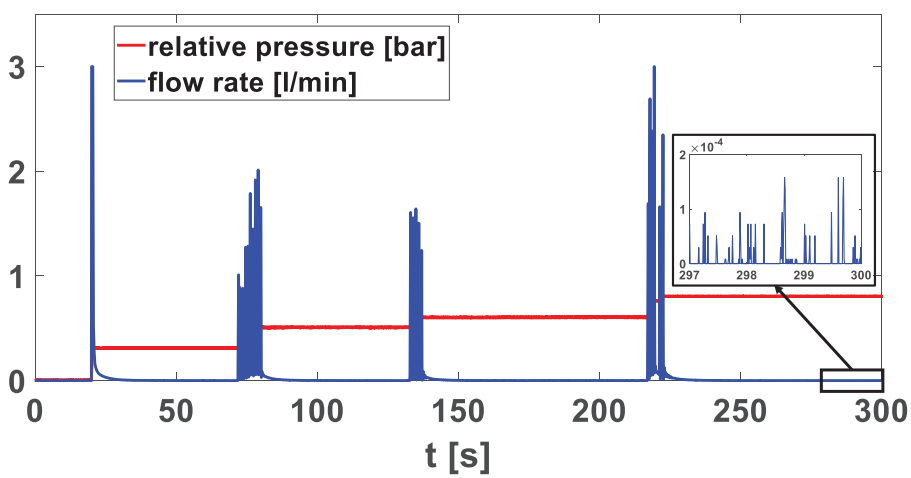


**Figure 9:** Post puncture leakage test.

*3.2. Mechanical tests*

Representative stress-strain curves at 0.1 mm/s, 1 mm/s obtained in the tensile experiments are presented in **Figure 10(a)**. They are related to a viscoelastic behavior, and the stress response clearly increases with the strain rate, given a certain strain value.
The stress relaxation tests with 5%, 25% and 50% deformations are also considered in **Figure 10(b)**, and the related stresses are normalized with respect to the initial peak value. Non-linear behavior is detectable, since the curves do not collapse into a single line and the normalized stress responses for different strain values do not coincide [36].

*3.3. Material constitutive equations*

The 1 mm/s tensile curve is used to derive the starting values of the Yeoh hyperelastic parameters (**Table 2**). On the other hand, the 25% strain relaxation test is exploited to compute a preliminary estimation of the Prony terms (**Table 3**).

**Table 2:** Initial guess for the Yeoh parameters.

| Parameter | Value |
|---|---|
| $C_{10}$ | 0.1578 |
| $C_{20}$ | $-3.4468 \cdot 10^{-3}$ |
| $C_{30}$ | $6.8532 \cdot 10^{-5}$ |
| $D_1$ | 0 |
| $D_2$ | 0 |
| $D_3$ | 0 |

**Table 3:** Initial guess for the Prony series terms.

| Index | $g_i$ [-] | $\tau_i$ [s] |
|---|---|---|
| **1** | 0.25505 | $9.30748 \cdot 10^{-2}$ |
| **2** | 0.23847 | 1.0255 |
| **3** | 0.26602 | 6.0801 |
| **4** | 0.16236 | 39.308 |
| **5** | $6.50798 \cdot 10^{-2}$ | 418.98 |
| ∞ | 0.01302 | - |

Comparison between the optimization results and the experimental curves is illustrated in **Figure 10**, while **Table 4** and **Table 5** list the optimized parameters. It is clear from **Table 3** and **Table 5** that no significant variation of the Prony terms is obtained from the optimization process.

Having all positive $C_{i0}$ values ensures hyperelastic stability, following Drucker's criterion for incompressible materials [33]:

$$d\sigma : d\varepsilon > 0 \tag{8}$$

Even if the actual material behavior is nonlinear, the introduced linear viscoelasticity approximation is able to excellently fit both the 0.1 mm/s and 1 mm/s tensile curves (**Figure 10 (a)**), in addition to good fitting of the 25% stress relaxation curve (**Figure 10 (b)**). Nevertheless, since the Prony-Yeoh approximation completely neglects nonlinearities, it may not be suitable for curves with lower and especially higher strain rates. In that case it would be necessary to consider a nonlinear viscoelastic model [33] [37]**.**
In any case, the considered model is very good for the purposes presented in this study, as the analyzed solicitations belong to the deformation range related to the performed and simulated puncture tests.

**Table 4:** Optimized Yeoh parameters.

| Model | Parameter | Initial value | Optimized value |
|---|---|---|---|
| **Yeoh** | $C_{10}$ | 0.1578 | 0.4765 |
| | $C_{20}$ | $-3.4468 \cdot 10^{-3}$ | 0.0013 |
| | $C_{30}$ | $6.8532 \cdot 10^{-5}$ | $3.38 \cdot 10^{-5}$ |

**Table 5:** Optimized Prony series terms.

| Index | $g_i$ [-] | $\tau_i$ [s] |
|---|---|---|
| **1** | 0.25505 | $9.30748 \cdot 10^{-2}$ |
| **2** | 0.23847 | 1.0255 |
| **3** | 0.26602 | 6.0801 |
| **4** | 0.16236 | 39.308 |
| **5** | $6.50798 \cdot 10^{-2}$ | 418.98 |
| ∞ | 0.01302 | - |

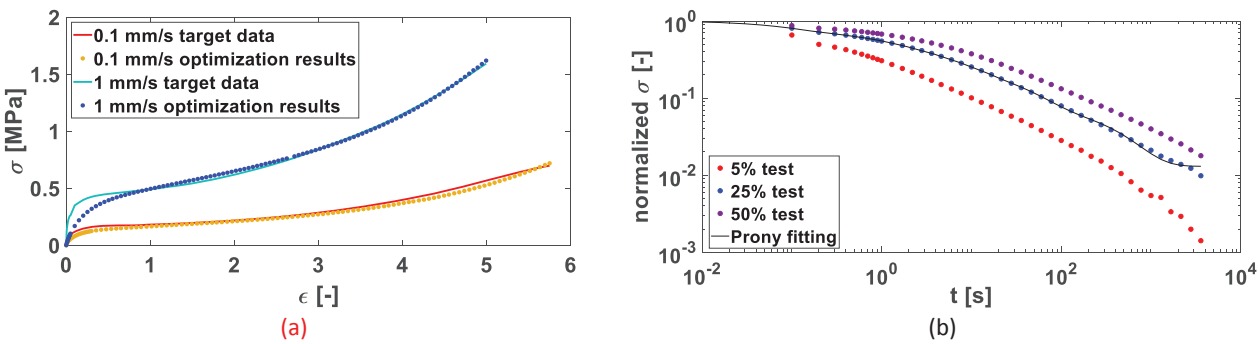


**Figure 10:** Comparison between tests and optimization results for the (a) hyperelastic and the (b) viscoelastic part.

*3.4. Puncture simulation results*

The complete history of the simulated radial displacement is shown in **Figure 11**. Time steps 1 (displacement imposition up to 0.8 mm with linear variation in time) and 2 (imposition of constant displacement of 0.8 mm) are included, even though the most important part is related to the decaying behavior after the removal of the boundary conditions (step 3), which represents the self-healing response.

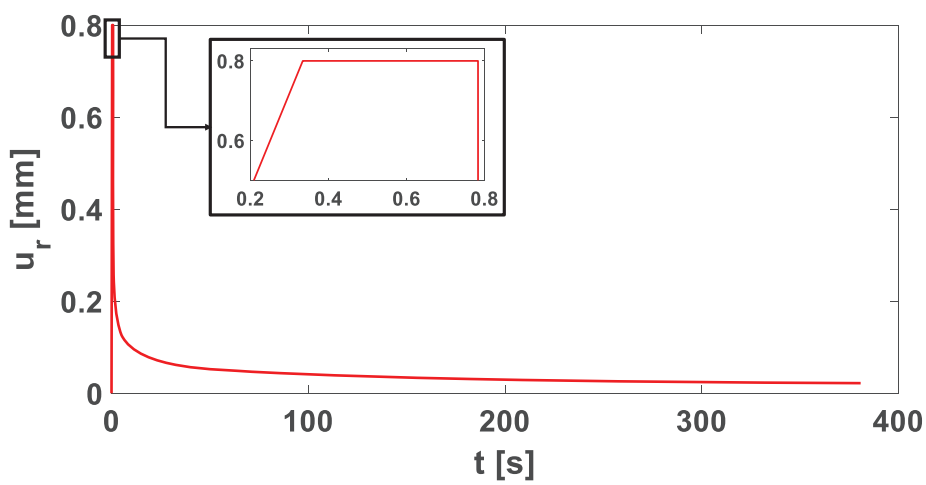


**Figure 11:** Simulated radial displacement history.

After simulation completion the radial displacement's history in the third step is exported and used to compute the volumetric flow rate of air:

$$Q(t) = \frac{\dot{m}(t)}{\rho_a} \tag{9}$$

$\rho_a = 1.225$ kg/m³ is the air density, $\dot{m}(t)$ indicates the mass flow rate through the puncture hole [38]:

$$\dot{m}(t) = C_d \cdot A_h(t) \cdot \psi \cdot p_0 \cdot \sqrt{\frac{2}{R_a \cdot T_0}} \tag{10}$$

The discharge coefficient $C_d$ is set to the typical 0.6 value for small orifices [38]; $p_0 = 0.131325$ MPa and $T_0 = 298.15$ K indicate air absolute pressure and temperature inside the cylindrical vessel used in the puncture test. $R_a = 287$ J/kg/K is the gas constant of air, while $\psi$ indicates the pressure dependent outflow function [38]:

$$\psi = \sqrt{\frac{\gamma}{\gamma - 1} \cdot \left[ \left(\frac{p_a}{p_0}\right)^{\frac{2}{\gamma}} - \left(\frac{p_a}{p_0}\right)^{\frac{\gamma+1}{\gamma}} \right]} \tag{11}$$

where $\gamma = 1.4$ is the specific heat ratio of air, and $p_a = 0.101325$ MPa is the ambient pressure. $A_h(t)$ is the equivalent area through which the air flows, in mm²; it varies in time since it depends on the puncture radius. Due to the introduced approximations null displacement and flow rate don't correspond to initial zero radius, but rather to $r = 0.2$ mm. The real hole area is consequently different from the considered $A_h(t)$ value (**Figure 12**):

$$A_h(t) = \pi \cdot [(r(t)^2 - a^2)] \tag{12}$$

$r(t) = a + u_r(t)$ is the hole radius, while $u_r(t)$ is the radial displacement from simulation.

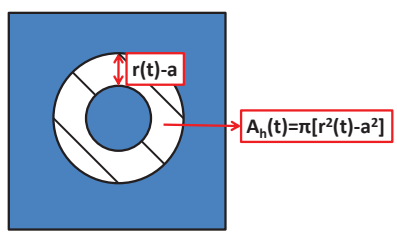


**Figure 12:** Equivalent hole area (dashed region).

The obtained $Q(t)$ is finally compared to the test data from the configuration without the aramid fabric, to analyze the material model's accuracy (**Figure 13**).

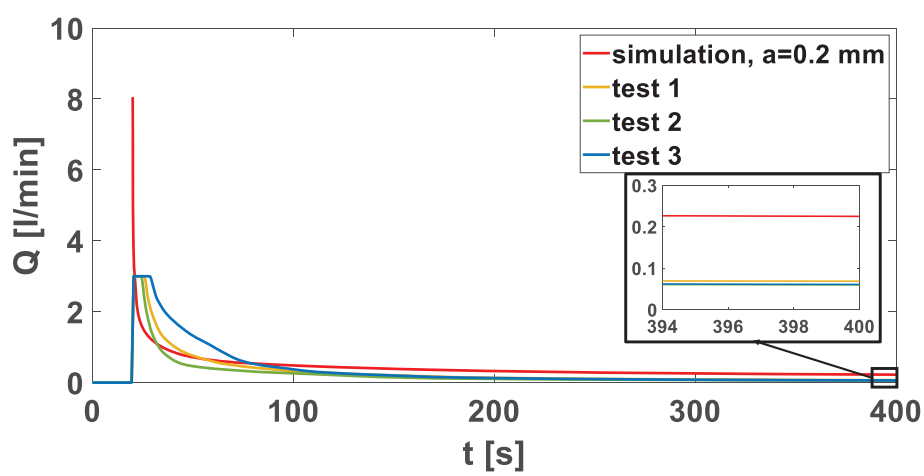


**Figure 13:** Comparison between simulated and experimental flow rate data.

## 4. Discussion

### *4.1. Puncture and healing response*

In the first configuration (supramolecular polymer between polyamide films), the self-healing response evaluated through the selected reference parameters appears rather repeatable. As a matter of fact, **Table 6** shows a very slight variation in the maximum and minimum flow rates and times between them from a test repetition to the other. More significant deviations are observed for the volume losses.
The flow meter reaches its saturation point immediately after puncture, and the material's performance is not optimal. The flow rate stabilizes around 0.06 l/min after approximately 400 s. The healing response is hence incomplete and relatively slow, leading to a significant loss of air volume.

**Table 6:** First configuration experimental data.

| SH material without aramid fabric | Max. flow rate [l/min] | Min. flow rate after puncture [l/min] | Lost vol. in 180 s after peak flow rate [$cm^3$] | Time between max. and min. flow rate [s] |
|---|---|---|---|---|
| **Repetition 1** | 3.000 | 0.066 | 1585.100 | 398.190 |
| **Repetition 2** | 3.000 | 0.057 | 1198.100 | 400.000 |
| **Repetition 3** | 3.000 | 0.058 | 2047.400 | 400.000 |
| **Average** | 3.000 | 0.060 | 1610.200 | 399.397 |
| **Standard deviation** | 0 | 0.004 | 347.179 | 0.853 |

The second configuration (**Table 7**) mimics the EMU space suits stacking sequence and has enhanced healing performances with respect to the previous case. The role of the aramid fabric is crucial because it represents an additional help in terms of hole closure, thanks to its resistance to tearing [12]. It is very difficult to break its fibers that, if displaced by the puncheon's motion in the sample, tend to get back to their position after the puncheon itself is removed. Some yarns may also be pulled into the material during penetration and could further enhance the healing response. In addition to this, the fabric partially blocks the deformation of the material into convex shape, caused by the pressure difference between the cylindrical vessel and the external environment.
The related maximum flow rates remain below 3 l/min and in all cases complete sealing of the hole is reached. Volume losses are consistently lower than the ones from the first configuration (1-2 orders of magnitude), and in two cases out of three the null flow rate is reached in less than a minute. In these regards, healing is much faster than in the tensile tests that are classically presented in literature. This is explained by the fact that the loads related to the pressure difference acting on the samples during the puncture tests are different from and far below the stress thresholds characterizing rupture during tensile tests. For this reason, a small contact is sufficient to ensure sealing; effective healing is instead verified at a later time, as presented in the results section (**Figure 9**).
Higher variability is instead found in the maximum flow rate and time data.

**Table 7:** Second configuration experimental data.

| SH material with aramid fabric | Max. flow rate [l/min] | Min. flow rate after puncture [l/min] | Lost vol. in 180 s after peak flow rate [$cm^3$] | Time between max. and min. flow rate [s] |
|---|---|---|---|---|
| **Repetition 1** | 2.815 | 0 | 123.700 | 393.940 |
| **Repetition 2** | 1.769 | 0 | 46.000 | 52.300 |
| **Repetition 3** | 2.915 | 0 | 93.200 | 53.030 |
| **Average** | 2.500 | 0 | 87.633 | 166.423 |
| **Standard deviation** | 0.518 | 0 | 31.694 | 160.879 |

The material's response leading to the lowest volumetric loss is compared with results from previous studies [10]. NASA conducted a research on some silicone and urethane polymers showing promising self-healing characteristics; they were all laminated to a 220-denier polyester base cloth to increase their overall damage tolerance [10]. The most significant among these materials are listed in **Table 8**, along with the suit's bladder baseline and the here studied configuration with aramid fabric. A special emphasis is put on Sylgard® Q3-6636, a silicone gel with self-healing and pressure sensitive adhesive bonding properties. Conathane® EN-11 and TyrLyner® urethanes are also considered.
The lowest volume loss of the material under study is related to the sample configuration with aramid fabric, which also surpasses Sylgard®. As already discussed, adding the ripstop fabric layer to the sample improves the sealing response on all fronts and leads to complete healing, differently from the past studies. The material is very efficient and may be able to resist to higher pressures, as suggested by the leakage test in **Figure 9**. Nonetheless, Sylgard® remains the material with the lowest maximum flow rate and time required to move from this value to the minimum flow rate (**Table 8**). A certain similarity is also noted between the aramid layup, the bladder baseline and Conathane® for what concerns the maximum flow rate data.
It is though necessary to underline that the studied material's sample is quite thicker than the ones from the previous study, which are also built in a slightly different way. This should be considered for future and more precise comparisons.

**Table 8:** Comparison among lowest volume results and past studies [10].

| Material | Max. flow rate [l/min] | Min. flow rate after puncture [l/min] | Lost vol. in 180 s after peak flow rate [$cm^3$] | Time between max. and min. flow rate [s] |
|---|---|---|---|---|
| **Bladder** | 1.875 | 0.676 | 2632.080 | 300.000 |
| **Conathane®** | 1.743 | 0.086 | 444.790 | 312.000 |
| **TyrLyner® urethane** | 1.181 | 0.024 | 110.630 | 30.000 |
| **Sylgard®** | 0.022 | 0.021 | 64.640 | 8.000 |
| **SH material with aramid fabric** | 1.769 | 0 | 46.000 | 52.300 |

*4.2. Puncture simulation*

When comparing the simulated $Q(t)$ to the reference tests, it is found that the peak flow rate from simulation is higher than the experimental values (**Figure 13**). This may be due to the fact that interaction between the material and the puncture probe is ignored. Furthermore, the 2D approximation does not consider the specimen's thickness, along which the hole's radial variation is not homogeneous. In the actual case, the lower face is the first to be freed from the puncheon. While the latter is still moving through the specimen, the bottom hole end has been already partially closed due to the material's initial elastic response. Therefore, once the puncheon has been completely removed from the sample, the hole section on the lower face has experienced minor stress relaxation effects and is smaller than the hole sections in the upper layers. The real initial area through which air can flow is hence below the simulated one, leading to lower maximum flow rate values. Another aspect is that the probe-sample contact friction is not modeled. Indeed, due to grip interaction the probe tends to drag the polymer and the lower polyamide film inside the generated puncture, providing additional sealing effect. Finally, pressure acting on the specimen is another important factor that may influence sealing and is not simulated.
Nevertheless, the built model is already able to follow the effective material's behavior, providing understanding of its self-healing ability and leading to significant results for a preliminary analysis. Anyway, improvements could be introduced in future studies by considering a 3D model with nonlinear viscoelasticity, contact interaction and rupture. The action of pressure on the specimen and the polyamide film layers may also be added.

A parametric analysis on the dependence of flow rate on the final puncture dimensions is also performed (**Figure 14**). The previously described simulation is run multiple times with different displacements imposed

to the hole. It is assumed that both the puncture velocity and the ratio between the probe's height and radius remain constant.

$$\frac{h_p}{r_f} = \frac{3.53\ mm}{1\ mm} = 3.53 = const. \tag{13}$$

With this assumption the radial velocity does not change either. The considered relaxation time of 180 s is related to the interval in which the air volumetric loss is computed. The chosen final radius $r_f$ values are 0.5 mm, 0.8 mm, 1.2 mm, 1.5 mm and 2 mm, and the results are compared with the already described case with $r_f = 1$ mm. As expected, both maximum and minimum flow rate increase with $r_f$.

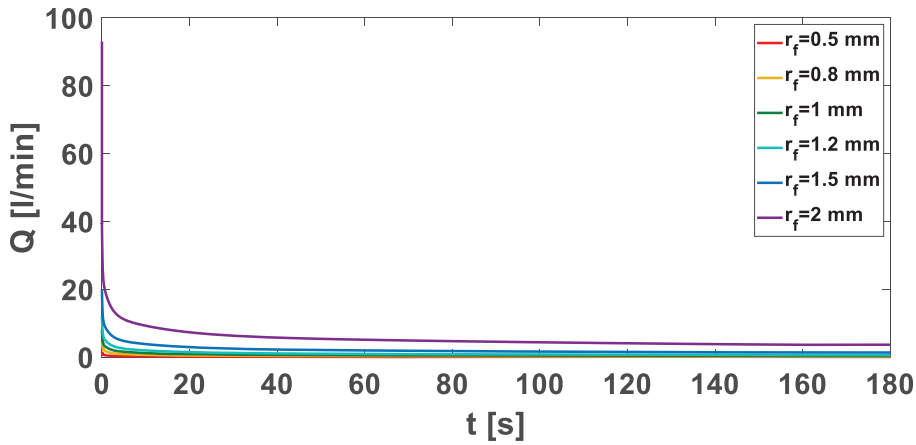


**Figure 14:** Parametric analysis of flow rate dependence on final puncture radius.

## 5. Conclusions

The investigated material shows reliable puncture response in both multilayer configurations with and without the aramid fabric, which additionally improves the sealing response. The maximum flow rate values are relatively consistent with data from previously analyzed materials considered for the specific space application, while superior performances are found both in terms of minimum flow rate and air volume losses in the case of the promising aramid fabric layup. The most significant and innovative aspect is that a null minimum flow rate is reached after puncture, differently from the other materials used as terms of comparison. Effective and complete healing and hole sealing are hence obtained. The high efficiency of the here introduced polymer and its ability to withstand relatively high pressures are also validated by the preformed leakage tests.

Concerning the material model, calibration of the viscoelastic and hyperelastic parameters leads to good results for the range of solicitations considered in the study and related to the performed puncture tests. Excellent prediction of the material's behavior and its effective self-healing ability is achieved. This is also supported by the coherence between puncture simulations and experimental data, observed through comparison of the two sets.
Nevertheless, several improvements will be necessary before being effectively able to apply the material to a functioning space system. Combination with a stiffer, more resistant supporting structure is necessary. Analysis of the interaction between the components would become fundamental in this case.
Another aspect is related to improvements to the testing apparatus and the experiments. Controlled puncture tests could be carried out in a vacuum chamber, and more accurate means to manufacture the specimens may be needed, along with the introduction of parts reproducing additional suit layers. A possible prototype with integration of the material may be also built for further characterization. An in-depth analysis of the effects of temperature and puncture velocity could also be performed by means of

tests in an environmental chamber. Finally, a nonlinear viscoelastic model could be useful to extend the study to higher and lower deformation rates.

**Acknowledgements**

This research has been partially supported by ASI (Italian Space Agency), grant agreement 2018-5-HH.0. ASI had no direct involvement in study design, collection analysis and interpretation of data, in the writing of the report and the decision to submit the article for publication. The authors want to acknowledge Ms. M.R. Pagano and Ms. M.R. Monzani for their support in the experimental activities. The authors are grateful to Arkema for having supplied the material.

**References**

[1] B. Alpert, B. Johnson, Extravehicular Activity Framework for Exploration - 2019, 49th Int. Conf. Environ. Syst. (2019).

[2] A. V. Degtyarev, L.M. Lobanov, A.P. Kushnar'ov, I.Y. Baranov, V.S. Volkov, A.O. Perepichay, V. V. Korotenko, O.A. Volkova, G.G. Osinovyy, Y.A. Lysenko, M.D. Kaliapin, On possibilities for development of the common-sense concept of habitats beyond the Earth, Acta Astronaut. 170 (2020) 487–498. https://doi.org/10.1016/j.actaastro.2020.02.014.

[3] D. Cadogan, C. Scheir, A. Dixit, J. Ware, E. Cooper, P. Kopf, Intelligent Flexible Materials for Deployable Space Structures (InFlex), 47th AIAA/ASME/ASCE/AHS/ASC Struct. Struct. Dyn. Mater. Conf. 14th AIAA/ASME/AHS Adapt. Struct. Conf. 7th. (2006) 1–17. https://doi.org/10.2514/6.2006-1897.

[4] M.Z. Naser, A.I. Chehab, Materials and design concepts for space-resilient structures, Prog. Aerosp. Sci. 98 (2018) 74–90. https://doi.org/10.1016/j.paerosci.2018.03.004.

[5] J. Ferl, J. Ware, D. Cadogan, J. Yavorsky, Self-Healing Technology for Gas Retention Structures and Space Suit Systems, 2007. https://doi.org/10.4271/2007-01-3211.

[6] E.P. Buslov, I.S. Komarov, V. V. Selivanov, V.A. Titov, N.A. Tovarnova, V.A. Feldstein, Protection of inflatable modules of orbital stations against impacts of particles of space debris, Acta Astronaut. 163 (2019) 54–61. https://doi.org/10.1016/j.actaastro.2019.04.046.

[7] I. Levchenko, K. Bazaka, T. Belmonte, M. Keidar, S. Xu, Advanced Materials for Next-Generation Spacecraft, Adv. Mater. 30 (2018) 1–13. https://doi.org/10.1002/adma.201802201.

[8] N.L. Skolnik, Z.R. Putnam, Evaluation of Dual Purpose Goop as a Candidate for Self-Healing Thermal Protection System Applications, (2020) 1–11. https://doi.org/10.2514/6.2020-0401.

[9] M.D. Hager, S. Van der Zwaag, U.S. Schubert, Self-healing materials, Springer, 2016.

[10] T.H. Fredrickson, NASA research announcement final report for space suit survivability enhancement, 1998.

[11] N.B. Moses, W.A. Crossley, An Approach To Self-Sealing Space Suit Design, in: 40th Int. Conf. Environ. Syst., 2010: p. 6246. https://doi.org/10.2514/6.2010-6246.

[12] E. Haddad, Y. Zhao, M. Celikin, M. Basti, K. Tagziria, E. Wallach, C. Semprimoschnig, U. Lafont, I. McKenzie, Mitigating the effect of space small debris on COPV in space with fiber sensors monitoring and self-repairing materials, (2019) 263. https://doi.org/10.1117/12.2536183.

[13] I.L. Hia, V. Vahedi, P. Pasbakhsh, Self-Healing Polymer Composites: Prospects, Challenges, and Applications, Polym. Rev. 56 (2016) 225–261. https://doi.org/10.1080/15583724.2015.1106555.

[14] M.D. Hager, P. Greil, C. Leyens, S. Van der Zwaag, U.S. Schubert, Self-healing materials, Adv. Mater. (2010).

[15] M. Chipara, J. Zaleski, B. Dragnea, E. Shansky, T. Onuta, M.D. Chipara, Self - Healing polymers for space applications, Collect. Tech. Pap. - AIAA/ASME/ASCE/AHS/ASC Struct. Struct. Dyn. Mater. Conf. 6 (2006) 4371–4379. https://doi.org/10.2514/6.2006-1946.

[16] B.A. Beiermann, M.W. Keller, N.R. Sottos, Self-healing flexible laminates for resealing of puncture damage, Smart Mater. Struct. 18 (2009). https://doi.org/10.1088/0964-1726/18/8/085001.

[17] E.J. Brandon, M. Vozoff, E.A. Kolawa, G.F. Studor, F. Lyons, M.W. Keller, B. Beiermann, S.R. White, N.R. Sottos, M.A. Curry, D.L. Banks, R. Brocato, L. Zhou, S. Jung, T.N. Jackson, K. Champaigne, Structural health management technologies for inflatable/deployable structures: Integrating sensing and self-healing, Acta Astronaut. 68 (2011) 883–903. https://doi.org/10.1016/j.actaastro.2010.08.016.

[18] H.R. Fischer, K. Tempelaars, A. Kerpershoek, T. Dingemans, M. Iqbal, H. Van Lonkhuyzen, B. Iwanowsky, C. Semprimoschnig, Development of flexible LEO-resistant PI films for space applications using a self-healing mechanism by surface-directed phase separation of block copolymers, ACS Appl. Mater. Interfaces. 2 (2010) 2218–2225. https://doi.org/10.1021/am100223v.

[19] X.F. Lei, Y. Chen, H.P. Zhang, X.J. Li, P. Yao, Q.Y. Zhang, Space survivable polyimides with excellent optical transparency and self-healing properties derived from hyperbranched polysiloxane, ACS Appl. Mater. Interfaces. 5 (2013) 10207–10220. https://doi.org/10.1021/am402957s.

[20] M. Rampf, O. Speck, T. Speck, R.H. Luchsinger, Investigation of a fast mechanical self-repair mechanism for inflatable structures, Int. J. Eng. Sci. 63 (2013) 61–70. https://doi.org/10.1016/j.ijengsci.2012.11.002.

[21] J.A. Syrett, C.R. Becer, D.M. Haddleton, Self-healing and self-mendable polymers, Polym. Chem. 1 (2010) 978–987. https://doi.org/10.1039/c0py00104j.

[22] M.A. Khalily, M. Goktas, M.O. Guler, Tuning viscoelastic properties of supramolecular peptide gels via dynamic covalent crosslinking, Org. Biomol. Chem. 13 (2015) 1983–1987. https://doi.org/10.1039/c4ob02217c.

[23] A. Phadke, C. Zhang, B. Arman, C.-C. Hsu, R.A. Mashelkar, A.K. Lele, M.J. Tauber, G. Arya, S. Varghese, Rapid self-healing hydrogels, Proc. Natl. Acad. Sci. 109 (2012) 4383–4388. https://doi.org/10.1073/pnas.1201122109.

[24] A.M. Grande, S.J. Garcia, S. Van Der Zwaag, On the interfacial healing of a supramolecular elastomer, Polymer (Guildf). 56 (2015) 435–442. https://doi.org/10.1016/j.polymer.2014.11.052.

[25] S.R. Zavada, N.R. McHardy, K.L. Gordon, T.F. Scott, Rapid, Puncture-Initiated Healing via Oxygen-Mediated Polymerization, ACS Macro Lett. 4 (2015) 819–824. https://doi.org/10.1021/acsmacrolett.5b00315.

[26] R.C.R. Gergely, W.A. Santa Cruz, B.P. Krull, E.L. Pruitt, J. Wang, N.R. Sottos, S.R. White, Restoration of Impact Damage in Polymers via a Hybrid Microcapsule–Microvascular Self-Healing System, Adv. Funct. Mater. 28 (2018) 35–39. https://doi.org/10.1002/adfm.201704197.

[27] N.J. Kanu, E. Gupta, U.K. Vates, G.K. Singh, Self-healing composites: A state-of-the-art review, Compos. Part A Appl. Sci. Manuf. 121 (2019) 474–486. https://doi.org/10.1016/j.compositesa.2019.04.012.

[28] F. Sordo, V. Michaud, Flexible Supramolecular Matrix Based Self-Healing Composites, Proc. Int. Conf.

Self-Healing Mater. (2013) 260–263.

[29] D. Montarnal, F. Tournilhac, M. Hidalgo, L. Leibler, Epoxy-based networks combining chemical and supramolecular hydrogen-bonding crosslinks, J. Polym. Sci. Part A Polym. Chem. 48 (2010) 1133–1141. https://doi.org/10.1002/pola.

[30] F. Sordo, S.J. Mougnier, N. Loureiro, F. Tournilhac, V. Michaud, Design of Self-Healing Supramolecular Rubbers with a Tunable Number of Chemical Cross-Links, Macromolecules. 48 (2015) 4394–4402. https://doi.org/10.1021/acs.macromol.5b00747.

[31] C.D. Cwalina, R.D. Dombrowski, C.J. McCutcheon, E.L. Christiansen, N.J. Wagner, MMOD puncture resistance of EVA suits with shear thickening fluid (STF) - Armortm absorber layers, Procedia Eng. 103 (2015) 97–104. https://doi.org/10.1016/j.proeng.2015.04.014.

[32] D.P. Gon, P. Paul, Complex Garment Systems to Survive in Outer Space, J. Text. Apparel, Technol. Manag. 7 (2011) 1–25.

[33] Abaqus analysis user's guide, Dassault Systèmes. (2015).

[34] S. Connolly, D. Mackenzie, T. Comlekci, Multi-objective optimization of hyperelastic material constants: A feasibility study, Const. Model. Rubber X - Proc. 10th Eur. Conf. Const. Model. Rubber, ECCMR X 2017. (2017) 273–278. https://doi.org/10.1201/9781315223278-47.

[35] Standard Test Method for Protective Clothing Material Resistance to Puncture, (2013). https://doi.org/10.1520/F1342-05R13.Copyright.

[36] C.A. Tweedie, K.J. Van Vliet, Contact creep compliance of viscoelastic materials via nanoindentation, J. Mater. Res. 21 (2006) 1576–1589. https://doi.org/10.1557/jmr.2006.0197.

[37] B. Nandi, T. Dalrymple, J. Yao, I. Lapczyk, Importance of Capturing Non-linear Viscoelastic Material Behavior in Tire Rolling Simulations, Meet. Tire Soc. (2014).

[38] M. Rampf, O. Speck, T. Speck, R.H. Luchsinger, Self-repairing membranes for inflatable structures inspired by a rapid wound sealing process of climbing plants, J. Bionic Eng. 8 (2011) 242–250. https://doi.org/10.1016/S1672-6529(11)60028-0.